

Henry Ford Health System

Henry Ford Health System Scholarly Commons

Orthopaedics Articles

Orthopaedics / Bone and Joint Center

3-12-2021

Measuring 3D In-vivo Shoulder Kinematics using Biplanar Videoradiography

Rebekah L. Lawrence

Roger Zael

Michael J. Bey

Follow this and additional works at: https://scholarlycommons.henryford.com/orthopaedics_articles

Measuring 3D In-vivo Shoulder Kinematics using Biplanar Videoradiography

Rebekah L. Lawrence¹, Roger Zuel¹, Michael J. Bey¹

¹ Bone and Joint Center, Department of Orthopaedic Surgery, Henry Ford Health System

Corresponding Author

Michael J. Bey

bey@bjc.hfh.edu

Citation

Lawrence, R.L., Zuel, R.,
Bey, M.J. Measuring 3D In-vivo
Shoulder Kinematics using Biplanar
Videoradiography. *J. Vis. Exp.* (169),
e62210, doi:10.3791/62210 (2021).

Date Published

March 12, 2021

DOI

10.3791/62210

URL

jove.com/video/62210

Abstract

The shoulder is one of the human body's most complex joint systems, with motion occurring through the coordinated actions of four individual joints, multiple ligaments, and approximately 20 muscles. Unfortunately, shoulder pathologies (e.g., rotator cuff tears, joint dislocations, arthritis) are common, resulting in substantial pain, disability, and decreased quality of life. The specific etiology for many of these pathologic conditions is not fully understood, but it is generally accepted that shoulder pathology is often associated with altered joint motion. Unfortunately, measuring shoulder motion with the necessary level of accuracy to investigate motion-based hypotheses is not trivial. However, radiographic-based motion measurement techniques have provided the advancement necessary to investigate motion-based hypotheses and provide a mechanistic understanding of shoulder function. Thus, the purpose of this article is to describe the approaches for measuring shoulder motion using a custom biplanar videoradiography system. The specific objectives of this article are to describe the protocols to acquire biplanar videoradiographic images of the shoulder complex, acquire CT scans, develop 3D bone models, locate anatomical landmarks, track the position and orientation of the humerus, scapula, and torso from the biplanar radiographic images, and calculate the kinematic outcome measures. In addition, the article will describe special considerations unique to the shoulder when measuring joint kinematics using this approach.

Introduction

The shoulder is one of the human body's most complex joint systems, with motion occurring through the coordinated actions of four individual joints, multiple ligaments, and approximately 20 muscles. The shoulder also has the greatest range of motion of the body's major joints and

is often described as a compromise between mobility and stability. Unfortunately, shoulder pathologies are common, resulting in substantial pain, disability, and decreased quality of life. For example, rotator cuff tears affect about 40% of the population over age 60^{1,2,3}, with approximately 250,000

rotator cuff repairs performed annually⁴, and an estimated economic burden of \$3-5 billion per year in the United States⁵. Additionally, shoulder dislocations are common and are often associated with chronic dysfunction⁶. Lastly, glenohumeral joint osteoarthritis (OA) is another significant clinical problem involving the shoulder, with population studies indicating that roughly 15%-20% of adults over the age of 65 have radiographic evidence of glenohumeral OA^{7,8}. These conditions are painful, impair activity levels, and decrease quality of life.

Although the pathogenesis of these conditions are not fully understood, it is generally accepted that altered shoulder motion is associated with many shoulder pathologies^{9,10,11}. Specifically, abnormal joint motion may contribute to the pathology^{9,12}, or that the pathology may lead to abnormal joint motion^{13,14}. Relationships between joint motion and pathology are likely complex, and subtle alterations in joint motion may be important in the shoulder. For example, although angular motion is the predominant motion occurring at the glenohumeral joint, joint translations also occur during shoulder motion. Under normal conditions these translations likely do not exceed several millimeters^{15,16,17,18,19}, and therefore may be below the level of in-vivo accuracy for some measurement techniques. While it may be tempting to assume that small deviations in joint motion may have little clinical impact, it is important to also recognize that the cumulative effect of subtle deviations over years of shoulder activity may exceed the individual's threshold for tissue healing and repair. Furthermore, in-vivo forces at the glenohumeral joint are not inconsequential. Using custom instrumented glenohumeral joint implants, previous studies have shown that raising a 2 kg weight to head height with an outstretched arm can result in glenohumeral joint forces that can range from 70% to 238% of body weight^{20,21,22}.

Consequently, the combination of subtle changes in joint motion and high forces concentrated over the glenoid's small load-bearing surface area may contribute to the development of degenerative shoulder pathologies.

Historically, the measurement of shoulder motion has been accomplished through a variety of experimental approaches. These approaches have included the use of complex cadaveric testing systems designed to simulate shoulder motion^{23,24,25,26,27}, video-based motion capture systems with surface markers^{28,29,31}, surface-mounted electromagnetic sensors^{32,33,34,35}, bone pins with reflective markers or other sensors attached^{36,37,38}, static two-dimensional medical imaging (i.e., fluoroscopy^{39,40,41} and radiographs^{17,42,43,44,45}), static three-dimensional (3D) medical imaging using MRI^{46,47}, computed tomography⁴⁸, and dynamic, 3D single plane fluoroscopic imaging^{49,50,51}. More recently, wearable sensors (e.g., inertial measurement units) have gained popularity for measuring shoulder motion outside the laboratory setting and in free-living conditions^{52,53,54,55,56,57}.

In recent years, there has been a proliferation of biplane radiographic or fluoroscopic systems designed to accurately measure dynamic, 3D in-vivo motions of the shoulder^{58,59,60,61,62}. The purpose of this article is to describe the authors' approach for measuring shoulder motion using a custom biplanar videoradiography system. The specific objectives of this article are to describe the protocols to acquire biplanar videoradiographic images of the shoulder complex, acquire CT scans, develop 3D bone models, locate anatomical landmarks, track the position and orientation of the humerus, scapula, and torso from the biplanar radiographic images, and calculate kinematic outcome measures.

Protocol

Prior to data collection, the participant provided written informed consent. The investigation was approved by Henry Ford Health System's Institutional Review Board.

Protocols for acquiring, processing, and analyzing biplane radiographic motion data are highly dependent upon the imaging systems, data processing software, and outcome measures of interest. The following protocol was specifically designed to track the scapula, humerus, and the third and the fourth ribs during scapular-plane or coronal-plane abduction and to quantify glenohumeral, scapulothoracic, and humerothoracic kinematics.

1. CT imaging protocol

1. Ask the participant to lie supine onto the CT examination table with their arms at their sides. Depending on the participant's size, position them off center on the table such that the entire hemi-torso is available for imaging.
2. To acquire the scout images, the technologist ensures that the CT field of view includes the clavicle (superiorly), the distal humeral epicondyles (inferiorly), the entire glenohumeral joint (laterally), and the costovertebral and sternocostal joints (medially) (**Figure 1**).
3. Acquire the CT scan with the following parameters: scan mode = helical; tube voltage = 120 kVp; tube current: 200-400 mA (auto); slice thickness = 0.66 mm; FOV = 34 cm.
4. Verify the scan quality and the field of view.
5. Reformat the acquisition using an image matrix size of 512 x 512 pixels. Given the slice thickness and FOV,

the acquisition results in an isotropic voxel spacing of approximately 0.66 mm.

6. Export the images in DICOM format.

2. Biplane X-ray motion capture protocol

NOTE: The custom biplanar x-ray system used in this protocol is described in the **Table of Materials**. Data collection procedures will likely vary with different system components. The x-ray systems are arbitrarily termed "green" and "red" to distinguish procedures and resulting image sequences and are positioned with an approximately 50° inter-beam angle and a source-to-image distance (SID) of approximately 183 cm (**Figure 2**). A minimum of two research personnel are required for the data collection; one to operate the x-ray system and computer, and the other to instruct the research participant.

1. Camera software setup

1. Set the camera aperture to the default setting ($f/5.6$).

NOTE: This value depends on several factors, including camera, exposure time, ISO, and participant anthropometrics.

2. Open the camera software and load the study protocol to each camera (sampling rate: 60 Hz, exposure time: 1,100 μ s).

NOTE: The camera exposure time may vary depending on several factors, including camera, aperture setting, and radiographic exposure.

2. System warmup

NOTE: The x-ray tube's anode may become damaged if high-powered exposures are produced when it is cold. Therefore, the tubes should be warmed up by a series of low-energy exposures based on the manufacturer's recommendations.

1. On both the x-ray generator control panels, select **Vascular** setting. The pre-programmed vascular settings produce low energy exposures appropriate for the system warm-up (per system manufacturer).
 2. Set the exposure time on the pulse generator to 0.25 s.
 3. On the x-ray generator control panels, hold down the **PREP** buttons. **Preparation Delay** appears on the screen.
 4. Once both the screens read **Ready to Expose**, simultaneously press and hold the **EXPOSE** buttons.

NOTE: This will not produce x-rays, but only arms the system. X-ray production only occurs by depressing the foot pedal or hand-held triggers.
 5. Depress the **PREP** and **EXPOSE** buttons on both the control panels, and simultaneously depress and hold the foot pedal (or hand-held) to trigger the x-ray generator to produce x-rays.

NOTE: The x-rays are produced for the duration specified by the pulse generator (step 2.3.2) or until the pedal is released, whichever occurs first.
 6. Repeat the steps 2.2.2-2.2.5 until the x-ray tube's heat unit (HU) exceeds the level required by the manufacturer to acquire images (5% HU for our system).
3. Verify the camera synchronization and image focus.

NOTE: Verify the camera synchronization and focus by acquiring a set of test images of the distortion correction grid (see **Table of Materials**). Each image intensifier will be tested individually using the steps described below.
1. Place the distortion correction grid on the image intensifier.
 2. On both x-ray generator control panels, select the **Cardiac** setting, which is programmed to the default radiographic technique (70 kVp, 320 mA, 2 ms, and focal spot = 1.0 mm).

NOTE: The camera settings remain unchanged (sampling rate: 60 Hz, exposure time: 1,100 μ s).
 3. Set the pulse generator to 0.25 s.
 4. Initiate the camera acquisition through the camera software and acquire x-ray images as described previously in the steps 2.2.3-2.2.5.
 5. Preview the resulting images and determine the elapsed time from the trigger pulse for each system. If the difference in elapsed time between cameras is more than 2 μ s, determine which camera is firing late and specify a frame delay in the camera software to resolve the issue.
 6. Visually inspect the sharpness of the image to verify the camera focus. For objective assessment, analyze a profile line drawn across a bead within the distortion correction grid using image processing software (e.g., ImageJ). Specifically, inspect the slope of the pixel gray values along this profile line. A more negative slope ensures a sharper image (assuming radiographic image is inverted such that the bead is dark). If necessary, refocus the cameras and repeat the steps 2.3.3-2.3.6.
4. Research participant setup and positioning

NOTE: The research participant's positioning is highly dependent upon the bones being tracked and the motion being tested. Testing is typically performed with the research participant seated on a fixed chair (i.e., not

swivel or wheeled) to minimize the potential for changes in their position that may cause the shoulder to move outside the 3D imaging volume.

1. Position the chair in the biplane imaging volume so that the shoulder to be tested is centered approximately where the biplane x-ray beams intersect. This is a preliminary position. Adjust it based on the participant's anthropometrics, the motion to be tested, and the bones to be tracked.
2. Ask the participant to be seated in a comfortable upright posture with arms resting at his/her side.
3. Secure a lead-lined protective vest across the participant's torso to cover their abdomen and the contralateral shoulder and chest.
4. Set the preliminary height of the image intensifiers. To help inform this procedure, turn on the light within the system's x-ray source. Raise the system until the participant's shadow cast onto the image intensifier is at the level of their axilla.

NOTE: The source and image intensifier within each system are coupled to move together. Uncoupled systems will require additional alignment steps not described here.

5. Establish the preliminary height of the image intensifiers. Gently move the participant on their chair within the biplane image volume while watching their shadow cast onto each image intensifier.

NOTE: A good initial guess is to have the participant positioned such that the acromioclavicular joint is approximately at the center of both image intensifiers. This position is a reasonable initial guess for the current protocol, which requires the

visualization and tracking of the humerus, scapula, and two ribs during shoulder elevation.

6. Once the participant's position appears to be reasonable in both systems, keep the light source on and ask the participant to perform the motion to be tested. Ensure that the participant's shoulder remains within the radiographic field of view during the entire motion trial. If possible, collimate x-ray beams to reduce exposure.
7. Repeat steps 2.4.5-2.4.6 until it appears that the participant's setup within the image volume is appropriate.
8. Researcher #1: Return to the control room to run the x-ray control panels and cameras. Set the x-ray control panel to low power fluoroscopy mode (60 kVp, 3-4 mA) and the pulse generator to a 0.25 s acquisition.
9. Researcher #2: Explain to the participant that an image will be taken so that their position can be verified in the images and describe the series of events that will happen. Warn the participant about the sounds the system makes (e.g., clicks, hums) to prevent any apprehension. Don a lead-lined protective vest, retrieve the hand-held trigger, and move as far away from the x-ray sources as possible to minimize exposure while still maintaining a clear line of sight and communication with the participant. If possible, stand behind a lead-lined shield with a window.
10. Researcher #1 (in x-ray control room): Start the cameras and prime the x-ray control panel as described previously (steps 2.2.3-2.2.5). When the system is ready to expose, notify the researcher #2.

11. Researcher #2 (in lab): Indicate to the participant about image acquisition. Trigger the radiographic image acquisition using the hand-held remote trigger. Inform the participant that an image was taken and excuse yourself to the control room.
 12. Researcher #1 and #2 (in x-ray control room): Inspect the images. Focus only on the participant's position and the visibility of all bones to be tracked. If necessary, repeat steps 2.4.5-2.4.12 until the participant's position is satisfactory.
 13. Once the setup and positioning of the x-ray system is established, do not move the x-ray system during the data collection session unless new calibration and distortion correction images are collected for each configuration. Also, instruct the participant to move as little as possible for the duration of the data collection session to avoid having to repeat setup procedures.
5. Data collection: Static image acquisition
 1. Researcher #1 (in x-ray control room): Set the optimized radiographic technique on the x-ray control panel (based on preliminary testing). The radiographic protocol used here is 70 kVp, 320 mA, 2 ms, and focal spot = 1.0 mm, with the camera collecting at 60 Hz and an exposure time of 1,100 μ s. Set the pulse generator to 0.25 s.
NOTE: Inform the participant that the next image will be a formal image acquisition.
 2. Researcher #2 (in the lab): Inform the participant to sit upright with their arm resting at their side.
 3. Acquire an image as previously described (steps 2.4.8-2.4.11).
 4. Researchers #1 and #2 (in x-ray control room): Inspect the images. Focus on the image quality (i.e., brightness and contrast) and visibility of all necessary bones. If adjustments to the image quality are needed, determine the parameter to be modified (i.e., f-stop, camera exposure time, kVp, mA) and reacquire the static image.
NOTE: It is critical to always be mindful of how the dose is affected by the radiographic parameters.
 5. Repeat steps 2.5.1-2.5.4 until the image quality is acceptable, within the dose estimates approved by the IRB.
 6. Once the image quality is acceptable, inspect the images for technical quality (e.g., corrupt frames).
 7. After an acceptable static trial image acquisition, save the trial from each camera (e.g., "green_still.cine", "red_still.cine").
6. Data Collection: Dynamic image acquisition
 1. Researcher #1 (in x-ray control room): Maintain the same radiographic parameters from the static trial image. Set the pulse generator to a 2.0 s exposure.
 2. Researcher #2 (in the lab): Teach the participant the motion to be performed, including the plane and timing of the motion. Verify that the chair and the participant's clothing and/or lead-lined vest do not interfere with the shoulder motion. Practice the motion trial with the participant. Use the verbal cue "Ready...and...go" paced so that it takes 2 s (i.e., the duration of the motion trial) to help the participant pace the initiation and completion of the motion.
NOTE: It is critical that the participant understands the procedures and can consistently perform the

motion trial to avoid the unnecessary exposure associated with a failed trial.

3. Researcher #2 (in the lab): After sufficient practice, retrieve the hand-held remote trigger. Move to a safe place in the lab with a clear line of sight and communication with the research participant.
4. Researcher #1 (in x-ray control room): Reset the pulse generator to 2.0 s, start the cameras, and prime the x-ray control panel as described previously (steps 2.3.4-2.3.5). When the system is ready to expose, notify the researcher #2.
5. Researcher #2 (in lab): Ask the research participant, "Are you ready?" [wait for the affirmative response] "Ready...and...go." (paced, as before, so that it takes 2 s).
6. Researcher #2 (in lab): Manually trigger the x-ray system when the participant initiates arm motion.
NOTE: Although manually triggering based on visual motion risks omitting the onset of the motion trial, it prevents over-exposing the research participant in the event of a miscommunication or a delayed start.). Once the trial is complete, inform the participant that an image was taken and excuse yourself to the control room to inspect the images.
7. Researchers #1 and #2 (in x-ray control room): Inspect the trial images for quality (i.e., brightness and contrast) and technical condition (i.e., any corrupt frames) (**Figure 3**). Save the motion trials from each camera (e.g., "green_scapab1.cine", "red_scapab1.cine").
8. Repeat the steps 2.6.1-2.6.7 to collect all the motion trials within the approved radiation safety protocol.

7. Collect calibration images

NOTE: Radiographic image calibration results in the definition of the laboratory-based coordinate system, the position and orientation of each x-ray radiographic system relative to laboratory coordinate system, and intrinsic parameters that allow for the generation of digitally reconstructed radiographs (DRRs), which are used in the markerless tracking process. The calibration calculations are described in the step 3.4.1.

1. Maintain the same camera settings and radiographic technique settings used during the data collection.
 2. Set the pulse generator to a 0.5 s exposure.
 3. Position the calibration cube (see **Table of Materials**) in the middle of the imaging volume.
 4. Acquire and save the cube images (e.g., "green_cube.cine", "red_cube.cine").
8. Collect the images for distortion correction and nonuniformity correction.

NOTE: Radiographic image collected using an image intensifier are affected by intensity, nonuniformity⁶³, and distortion. Consequently, images of a white-field and distortion correction grid are acquired on each radiographic system to determine the corrections needed. It is generally prudent to collect calibration images before distortion and nonuniformity correction images in case the image intensifiers are bumped while the distortion grid is being positioned.

1. Remove all objects from the radiographic field of view.
2. Maintain the same camera settings and radiographic technique settings used during the data collection. Set the pulse generator to a 0.5 s exposure.

3. Attach the distortion correction grid (see **Table of Materials**) to the surface of the green image intensifier.
4. Acquire the grid and white-field images.
5. Save the images (e.g., "green_grid.cine", "red_white.cine").
6. Move the grid to the red image intensifier and repeat steps 2.7.2-2.7.5, modifying the image filenames, as appropriate.

3. Data processing protocol

NOTE: Procedures for preparing the bony geometry, image pre-processing (i.e., distortion and non-uniformity correction and image calibration), and markerless tracking are highly variable and depend on the software used. The procedures described herein are specific to the proprietary software. However, the major data processing steps are likely translatable to any x-ray motion capture software package.

1. Processing CT scan

NOTE: The proprietary markerless tracking software used by the authors' lab optimizes the position and orientation of a DRR. Therefore, the procedures for processing the CT scan results in the creation of a 16-bit TIFF image stack. Other software packages may require the bony geometry to be represented in different formats or specifications.

1. Open an image processing program (e.g., Mimics, FIJI) and import the CT images.
2. Segment the humerus from the surrounding soft tissues. For the ribs, create an extension that connects the anterior aspect of the rib to the

manubrium to digitize the sternocostal joint later in step 3.2.6.

3. Perform a Boolean operation on the finished mask with a black mask (i.e., all pixels are colored black) (operation: black minus bone). This results in an inverted mask of the bone in which all pixels are black except for those corresponding to the bone, which remain in CT grayscale.
 4. Crop the image stack along all three axes to eliminate the black (i.e., non-bone) pixels. Leave some black pixels at the edges of this 3D bounding box.
 5. Save the modified image stack in the TIFF format.
 6. Repeat the steps 3.1.1-3.1.5 for all the remaining bones.
- #### 2. Defining anatomical coordinate systems and regions of interest (ROIs)

NOTE: This protocol orients anatomical coordinate systems as follows. For a right shoulder, the +X axis is oriented laterally, the +Y axis is oriented superiorly, and the +Z axis is oriented posteriorly. For a left shoulder, the +X axis is oriented laterally, the +Y axis is oriented superiorly, and the +Z axis is oriented anteriorly.

1. Import the TIFF image stack for the bone to be processed. Convert the TIFF stack to a .RAW file and render a 3D bone model based on the known pixel dimensions and image spacing using the proprietary software.

NOTE: The resolution of the model is based on the sampling of the CT volume (i.e., voxel spacing). Consequently, the average area of the mesh triangles is approximately 1.02 mm^2 ($\pm 0.2 \text{ mm}^2$) (step 1.3).

2. Digitize the anatomical landmarks on the humerus as follows (**Figure 4A**).
 1. Geometric center of the humeral head: Determine the dimensions and position of a sphere that minimizes the distance between the sphere's surface and the humeral articular surface using a least-squares algorithm. Define the geometric center of the humeral head as the coordinates of the optimized sphere's center.
 2. Medial and lateral epicondyles: Located at the widest section of the distal humerus.
3. Define humeral head ROI as follows (**Figure 5A**).
 1. The entire humeral articular surface and greater tuberosity.
4. Digitize the anatomical landmarks on the scapula as follows (**Figure 4B**).
 1. Root of the scapular spine: Located at the medial border along the scapular spine.
 2. Posterior acromioclavicular joint: Located at the posterior aspect of the clavicular facet on the scapular acromion.
 3. Inferior angle: Located at the inferior-most point on the scapula.
5. Define scapular ROIs as follows (**Figure 5B**).
 1. Acromion: The undersurface of the acromion lateral to the spine of the scapula.
 2. Glenoid: The entire articulating surface of the glenoid.
6. Digitize anatomical landmarks on the ribs as follows (**Figure 4C**).
 1. Anterior rib: Located at the medial-most portion of the rib extension.
 2. Posterior rib: Located at the superior/inferior midpoint of the posterior aspect of the facet on the head of the rib.
 3. Lateral rib: Located at the lateral-most aspect of the rib when the anterior and posterior rib points are aligned vertically on the screen.
3. Image pre-processing

NOTE: Image pre-processing is performed using proprietary software and involves converting the cine image files to TIFF stacks and correcting the images for distortion nonuniformity.

 1. Perform non-uniformity correction: The software averages the approximately 30 frames (i.e., 0.5 s of data) to produce a single, high-quality, bright-field image to minimize the effect of noise in any single frame. The bright-field image is used to calculate the true radiographic density along the ray from the x-ray source to each pixel of each frame of data. The sum of the radiographic density of all the matter penetrated by each pixel's ray is proportional to the logarithm of the bright field for that pixel minus the logarithm of the observation image for that pixel (i.e., log-sub processing).
 2. Perform distortion correction: The software averages the approximately 30 frames (i.e., 0.5 second of data) to produce a single image and reduces the effect of noise in any individual image. The distortion correction software creates an affine map from each triple of adjacent bead positions in the distortion grid image to the known (true) position of those three beads in the Lucite distortion

correction grid. This collection of small affine maps is then used to resample each observed frame of the motion trial into the true coordinates represented by the orthogonal array of beads.

3. Apply distortion and non-uniformity corrections to all frames of each trial.
4. Biplane imaging volume calibration.

NOTE: Image calibration was performed using proprietary software. The software uses a nonlinear optimization algorithm to adjust the observed calibration object bead locations to their known 3D locations. This process is conducted for each set of biplanar calibration images. The result is a system that can digitally project two views of a bone volume and register them against radiographic images of the same bone collected during the data collection.

5. Markerless tracking

NOTE: Markerless tracking is performed using proprietary software. Software such as Autoscooper and C-Motion can also be used to complete this process.

1. On the first frame of the motion trial, rotate and translate the DRR using the software controls until it appears to match well to the biplane x-ray images (**Figure 6**).
2. Save the manual solution.
3. Apply the optimization algorithm.
4. Visually inspect the solution determined to be optimal by the algorithm based on the initial manual solution. If necessary, adjust the solution and repeat steps 3.5.2-3.5.3 until satisfied with the optimized solution.

5. Repeat steps 3.5.1-3.5.4 for every 10th frame across the motion trial.

NOTE: This interval is dependent upon several factors, including frame rate, motion speed, and image quality. Smaller intervals may be required.

6. Once every 10th frame is tracked, perform an optimization to create interpolated preliminary solutions that are subsequently optimized.
7. Continue to refine the solutions until all the frames of the motion trial are tracked well.

4. Data analysis protocol

NOTE: The proprietary markerless tracking software used in this protocol results in the raw and filtered trajectories of the anatomical landmarks that will be used to construct anatomical coordinate systems. These coordinates are expressed relative to the laboratory coordinate system defined by the calibration object during the calibration procedure. The following protocol describes, in general terms, the procedures for calculating kinematic outcome measures from these landmark trajectories such that they can be computed in any programming language (e.g., MATLAB). A second proprietary software is used to calculate kinematics and proximity statistics.

1. Calculate kinematics and proximity statistics

NOTE: The primary kinematic outcome measures include joint rotations (i.e., Euler angles) and positions. The primary proximity statistics include the minimum gap, average gap, and weighted-average contact center, which are calculated for every frame of data. Collectively, these measures describe joint arthrokinematics, or surface interactions during a movement. Anatomical proximities that are aggregated across the motion trial

include the average contact center, contact path, and contact path length.

1. For each bone and frame of motion, use the filtered anatomical landmark coordinates (i.e., output from the markerless tracking software) to construct a 16-element transformation matrix representing the bone's anatomical coordinate system relative to the laboratory coordinate system.
2. Calculate the relative kinematics by relating the anatomical coordinate systems between relevant bones using the software.
3. Extract the joint angles and positions using conventional methods⁶⁴. Given the orientation of the anatomical coordinate systems, extract the glenohumeral kinematics using a Z-X'-Y" rotation sequence, extract the scapulothoracic kinematics using a Y-Z'-X" rotation sequence, and extract the humerothoracic kinematics using a Y-Z'-Y" rotation sequence.
4. Minimum gap: Calculate the smallest gap (i.e., distance) between the centroids of the nearest-neighbor triangle on the opposite bone using the software.
5. Average gap: Calculate the area-weighted mean of the minimum gap using the triangles that have the smallest gap to their nearest neighbor within a specified measurement area using the software. Define the measurement area as the triangles closest to the opposite bone whose areas sum to 200 mm². Incorporate this measurement area in the calculation to ensure that only the surface that is reasonably near to the opposite bone is included in the average gap calculation.

NOTE: The sizes of the measurement area (i.e., 200 mm²) was selected during initial algorithm development after it was found to consistently reflect subacromial space and glenohumeral joint proximities without being overly biased from distant surfaces. Use of this measure for broader surface interactions (e.g., tibiofemoral) may require a larger measurement area.

6. Weighted-average contact center (i.e., centroid): Calculate the point on the ROI surface that minimizes the weighted distance to all other triangles within the measurement area (i.e., triangles closest to the opposite bone whose areas sum to 200 mm²) using the software. The weighting factor for each triangle in the measurement area is calculated as: triangle area / squared distance to nearest-neighbor centroid (i.e., inverse square weighting). In this way, the triangles that are weighted more heavily are larger (by a factor of 1) and closer to the opposite bone (by a factor of the squared minimum distance).
7. Average contact center: Calculate the average position of the contact center (i.e., centroid) across the motion trial using the software. Given contact centers represent joint arthrokinematics, the average contact center represents the center of surface interactions during a movement.
8. Contact path: Define by connecting the coordinates of the weighted-average contact center across the motion trial using the software.
9. Contact path length: Calculate the length of the contact path across the motion trial using the software.

Representative Results

A 52-year-old asymptomatic female (BMI = 23.6 kg/m²) was recruited as part of a previous investigation and underwent motion testing (coronal plane abduction) on her dominant (right) shoulder⁶⁵. Prior to data collection, the participant provided written informed consent. The investigation was approved by Henry Ford Health System's Institutional Review Board. Data collection was performed using the protocol previously described (**Figure 3**).

The participant's glenohumeral, scapulothoracic, and humerothoracic kinematics are presented in **Figure 7**, **Figure 8**, and **Figure 9**, respectively. Visual inspection of glenohumeral and scapulothoracic kinematics suggests the participant's shoulder motion was consistent with what is generally expected during coronal plane abduction⁶⁶. Specifically, glenohumeral motion consisted of elevation and slight external rotation, and was generally in a plane posterior to the scapula (**Figure 7**), while scapulothoracic motion consisted of upward rotation, posterior tilt, and slight internal/external rotation (**Figure 8**).

During the motion trial, the minimum subacromial distance (i.e., narrowest width of the subacromial outlet for a given frame) ranged from 1.8 mm at 74.0° humerothoracic elevation (frame 45) to 8.3 mm at 134.0° humerothoracic elevation (frame 89) (**Figure 10A**, **Figure 11A**). The average subacromial distance (i.e., average width of the subacromial outlet within the specified 200 mm² measurement area) tended to follow a similar trajectory as the minimum distance metric. For example, the average subacromial distance ranged from 4.2 mm at 75.4° humerothoracic elevation (frame

46) to 9.2 mm at 134.0° humerothoracic elevation (frame 89). Finally, the minimum subacromial distance tended to follow a complementary trajectory to the surface area metric (**Figure 10B**) such that the minimum distance tended to be smaller when the surface area is larger. Plotting the location of the minimum distance on the humeral head suggests the location closest to the acromion shifts laterally across the rotator cuff footprint as the humerothoracic elevation angle increases (**Figure 11A**). Across the motion trial, the contact path length measured 40.5 mm on the humeral head and 28.8 mm on the acromion.

During the motion trial, the minimum glenohumeral distance (i.e., narrowest width of the glenohumeral joint space) ranged from 1.0 mm at 137.9° humerothoracic elevation (frame 92) to 2.1 mm at 34.2° humerothoracic elevation (frame 21) (**Figure 12A**, **Figure 11B**). As with the subacromial distances, the average glenohumeral distance tended to follow a similar trajectory as the minimum distance metric, and these distances followed a complementary trajectory with the surface area metric (**Figure 12B**). For example, the average glenohumeral distance ranged from 1.4 mm at 137.9° humerothoracic elevation (frame 92) to 2.6 mm at 23.5° humerothoracic elevation (frame 12). Plotting the location of the glenohumeral contact center relative to the glenoid edge contours suggest that the participant's arthrokinematics included moderate surface interactions. Specifically, the humerus stayed relatively centered in the glenoid in the anterior/posterior direction but shifted superiorly and then inferiorly during the motion trial (**Figure 11B**). Across the motion trial, the contact path length measured 30.0 mm on the glenoid and 45.4 mm on the humeral head.

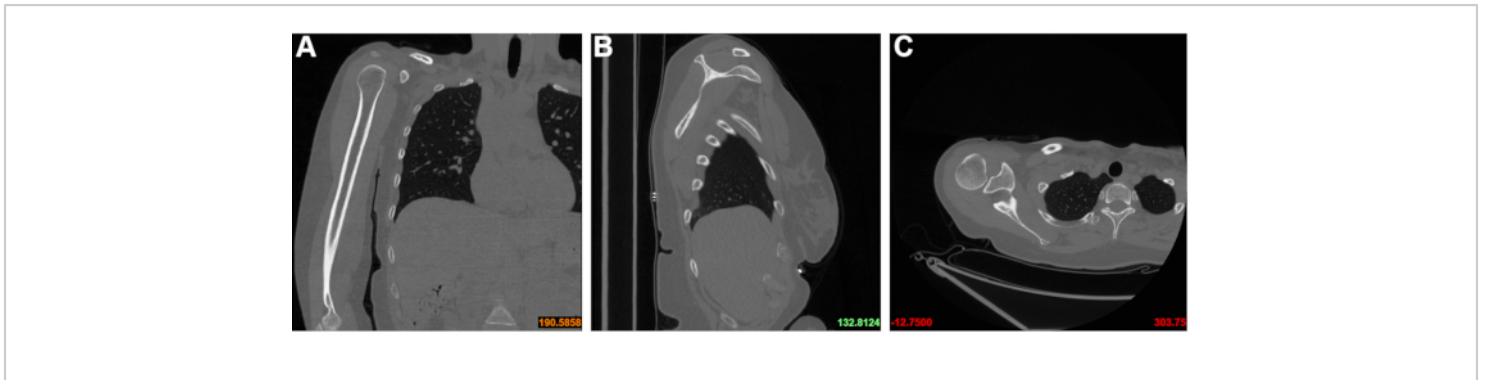


Figure 1: The CT field of view. (A) coronal, (B) sagittal, and (C) transverse planes. During acquisition, the CT technologist ensures the field of view includes the clavicle (superiorly), the distal humeral epicondyles (inferiorly), the entire glenohumeral joint (laterally), and the costovertebral and sternocostal joints (medially). [Please click here to view a larger version of this figure.](#)

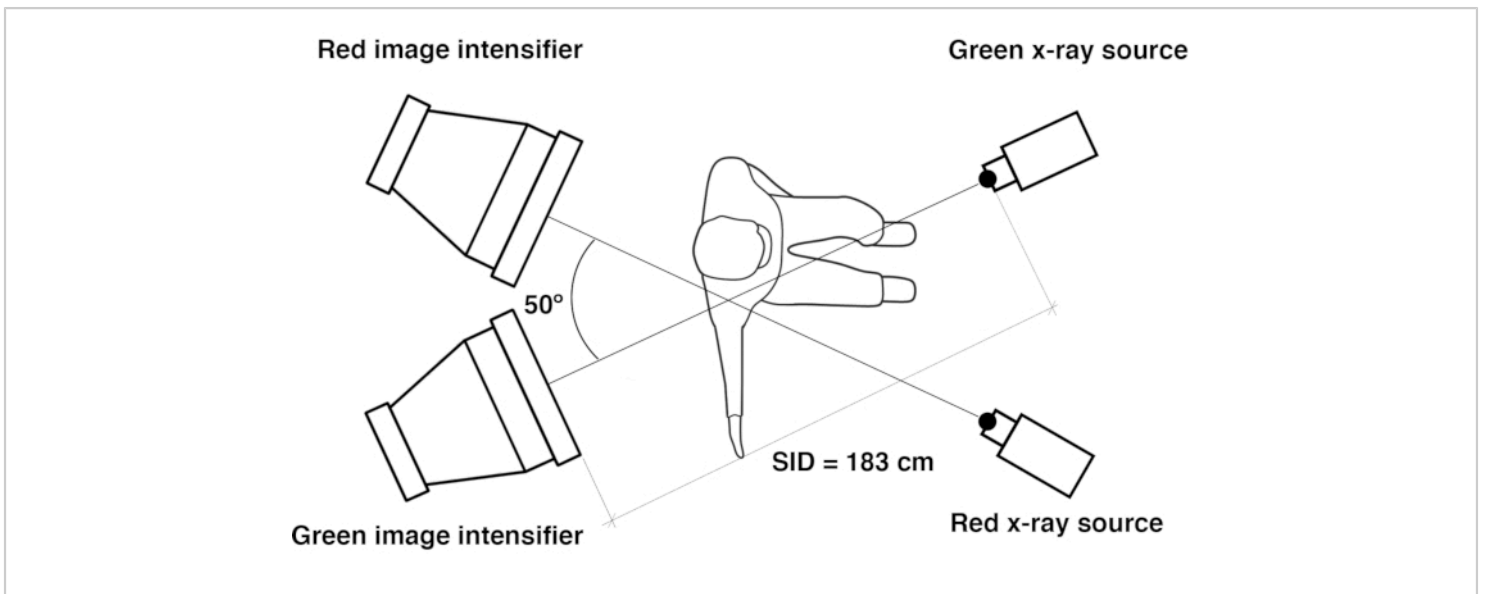


Figure 2: Schematic of the biplane videoradiographic system. The x-ray systems are positioned with a 50° inter-beam angle and a source-to-image distance (SID) of 183 cm. Participants are positioned in the biplane volume such that their glenohumeral joint is located approximately at the intersection of the x-ray beams. Systems are termed "green" and "red" to distinguish the control panels and the filenames of the images. [Please click here to view a larger version of this figure.](#)

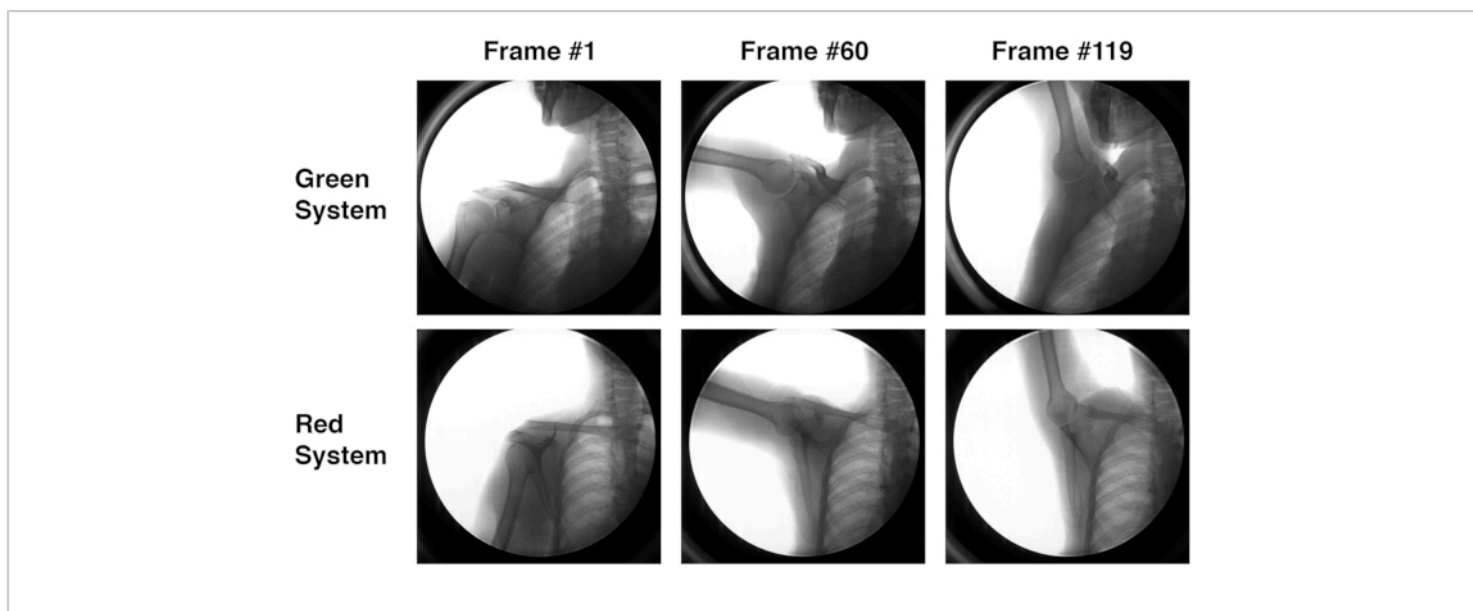


Figure 3: Biplane radiographic images from a representative subject during coronal plane abduction. Although the jaw appears in the images of the green system, care should be taken to avoid including the head in the field of view to minimize dose to this area. [Please click here to view a larger version of this figure.](#)

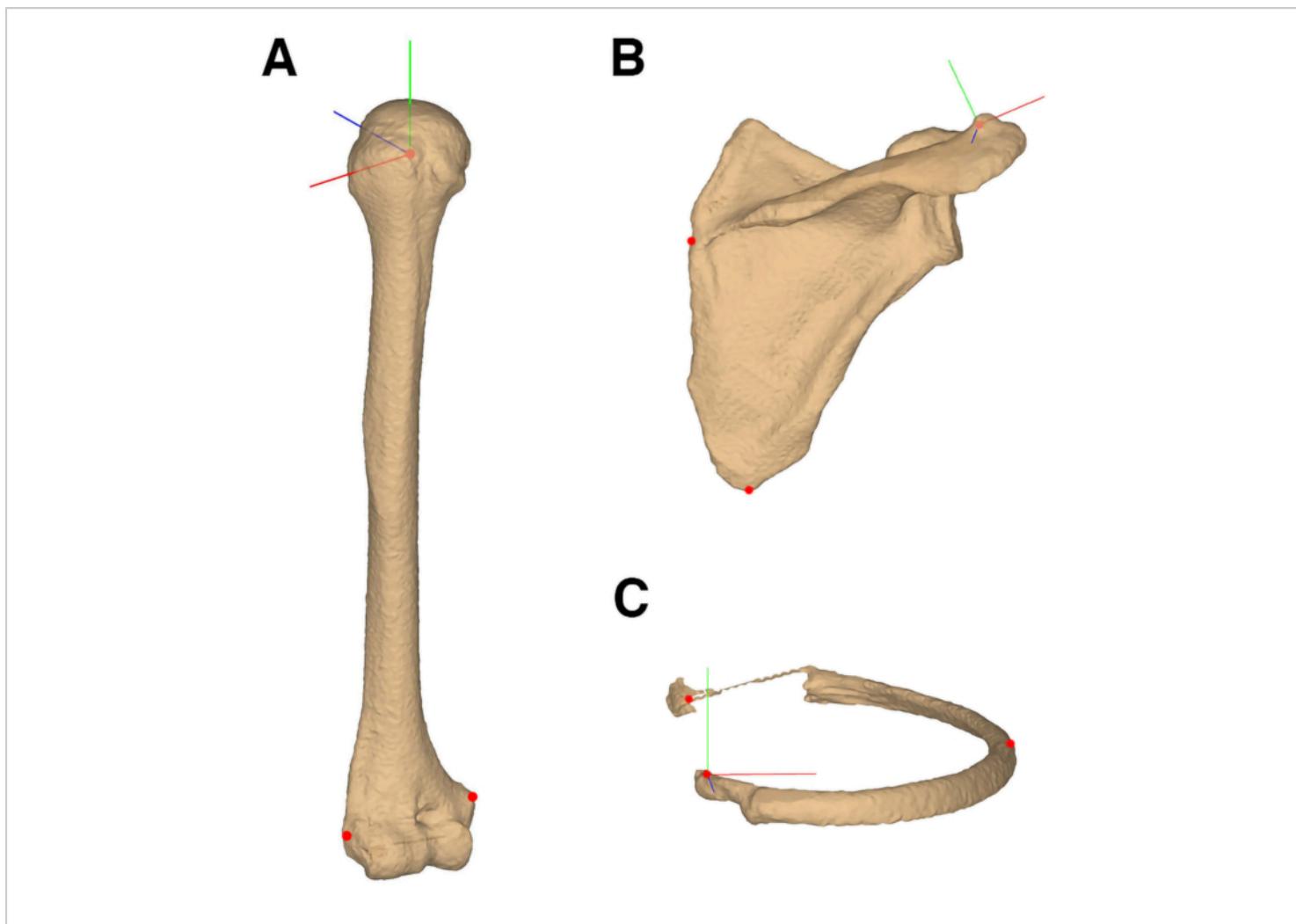


Figure 4: Definition of anatomical coordinate systems. (A) Humeral coordinate system defined by digitizing the geometric center of the humeral head, medial epicondyle, and lateral epicondyle. (B) Scapular coordinate system defined by digitizing the medial spine, inferior angle, and posterior aspect of the acromioclavicular joint. (C) Rib coordinate system defined by digitizing the posterior aspect of the costovertebral facet, the lateral-most aspect of the rib, and the lateral sternum at the level of the rib. [Please click here to view a larger version of this figure.](#)

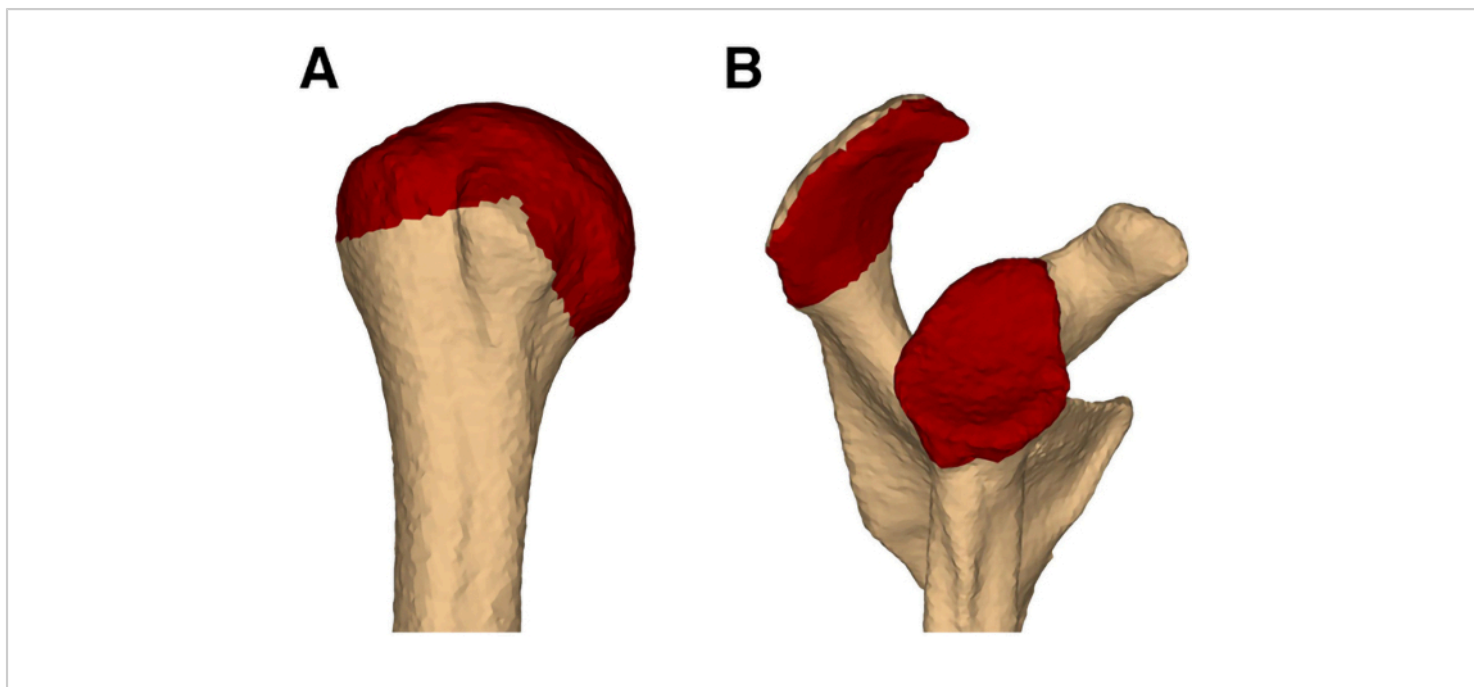


Figure 5: Definition of regions of interest (ROI) for proximity statistics. (A) humeral head ROI, which is used to calculate acromiohumeral distance and glenohumeral joint contact patterns, (B) acromial and glenoid ROIs, which are used to calculate acromiohumeral distance and glenohumeral joint contact patterns, respectively. [Please click here to view a larger version of this figure.](#)

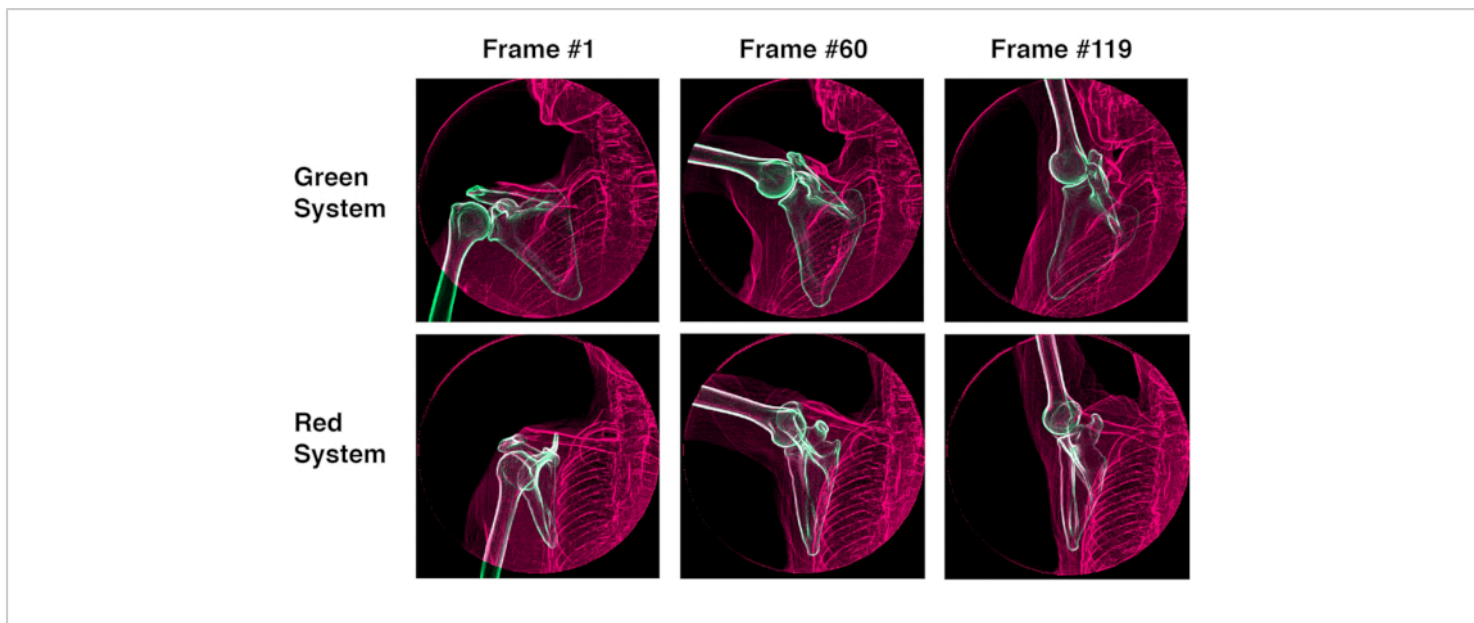


Figure 6: Screenshots of the proprietary markerless tracking software. The screenshot illustrates the optimized solutions of the humerus and scapula from a representative subject during coronal plane abduction. [Please click here to view a larger version of this figure.](#)

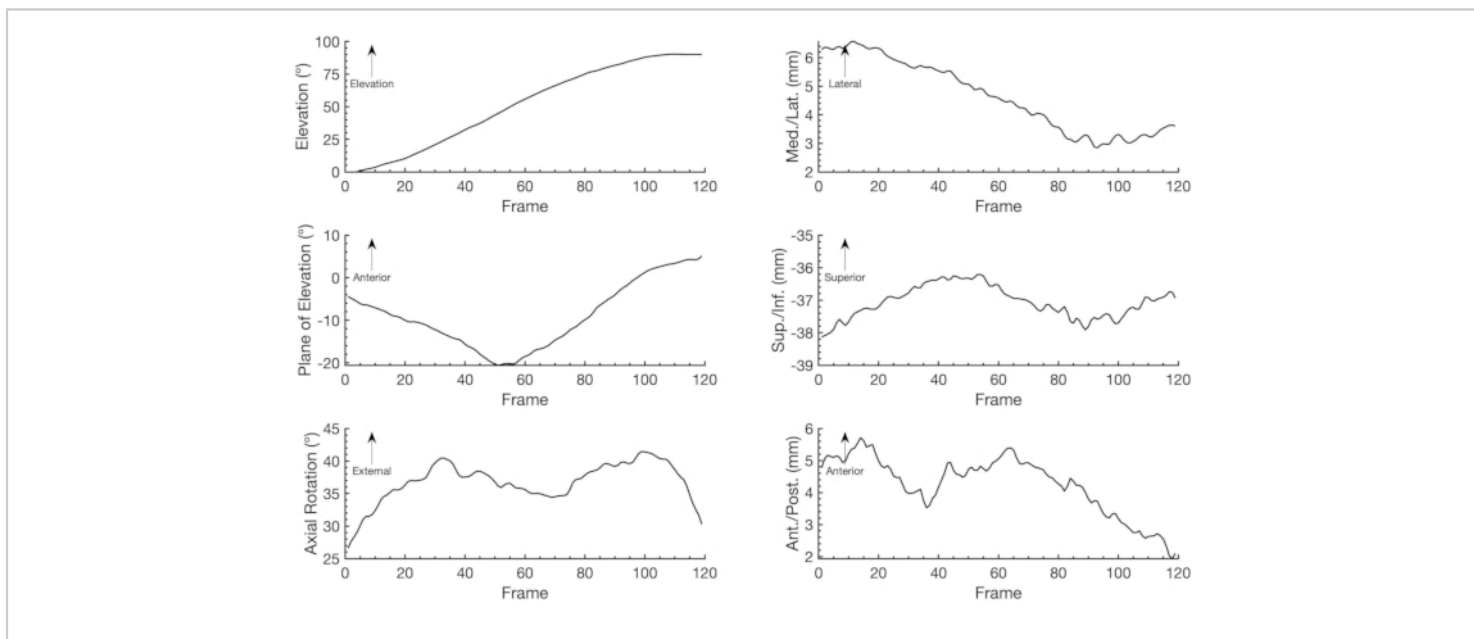


Figure 7: Glenohumeral kinematics from a representative subject during a single trial of coronal plane abduction.

Note: Anterior position has been transformed to be a positive value. Abbreviations: med. = medial; lat. = lateral; sup. = superior; inf. = inferior; ant. = anterior; post. = posterior. [Please click here to view a larger version of this figure.](#)

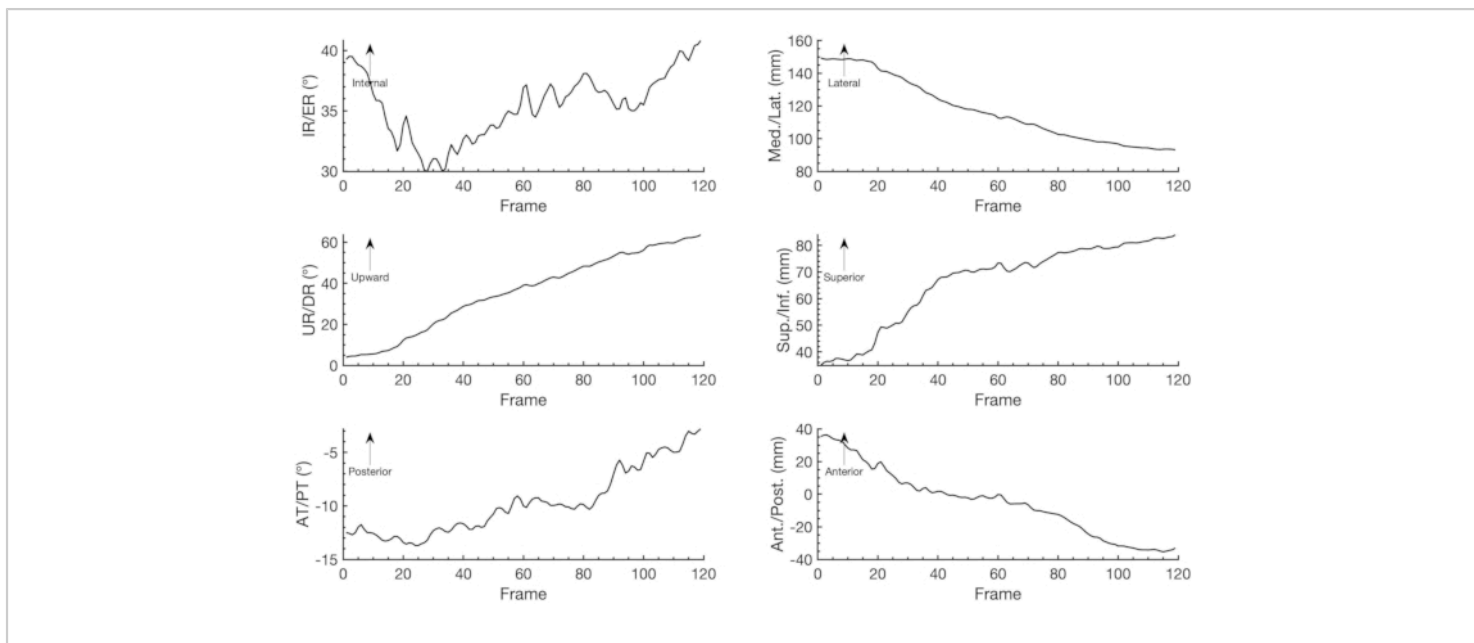


Figure 8: Scapulothoracic kinematics from a representative subject during a single trial of coronal plane abduction.

Note: Anterior position has been transformed to be a positive value. Abbreviations: IR = internal rotation; ER = external rotation; UR = upward rotation; DR = downward rotation; AT = anterior tilt; PT = posterior tilt; med. = medial; lat. = lateral; sup. = superior; inf. = inferior; ant. = anterior; post. = posterior. [Please click here to view a larger version of this figure.](#)

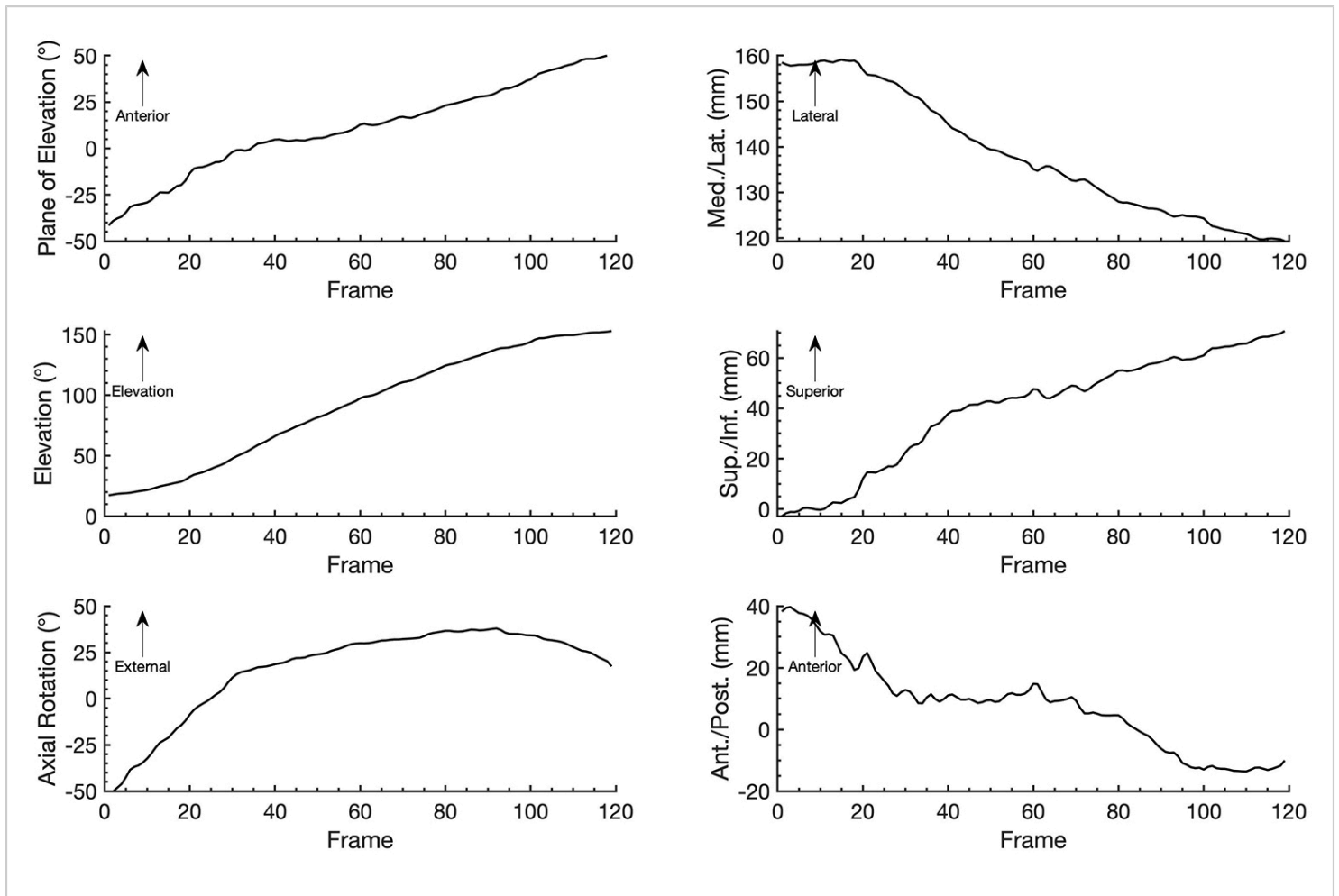


Figure 9: Humerothoracic kinematics from a representative subject during a single trial of coronal plane abduction.

Note: Anterior position has been transformed to be a positive value. Abbreviations: med. = medial; lat. = lateral; sup. = superior; inf. = inferior; ant. = anterior; post. = posterior. [Please click here to view a larger version of this figure.](#)

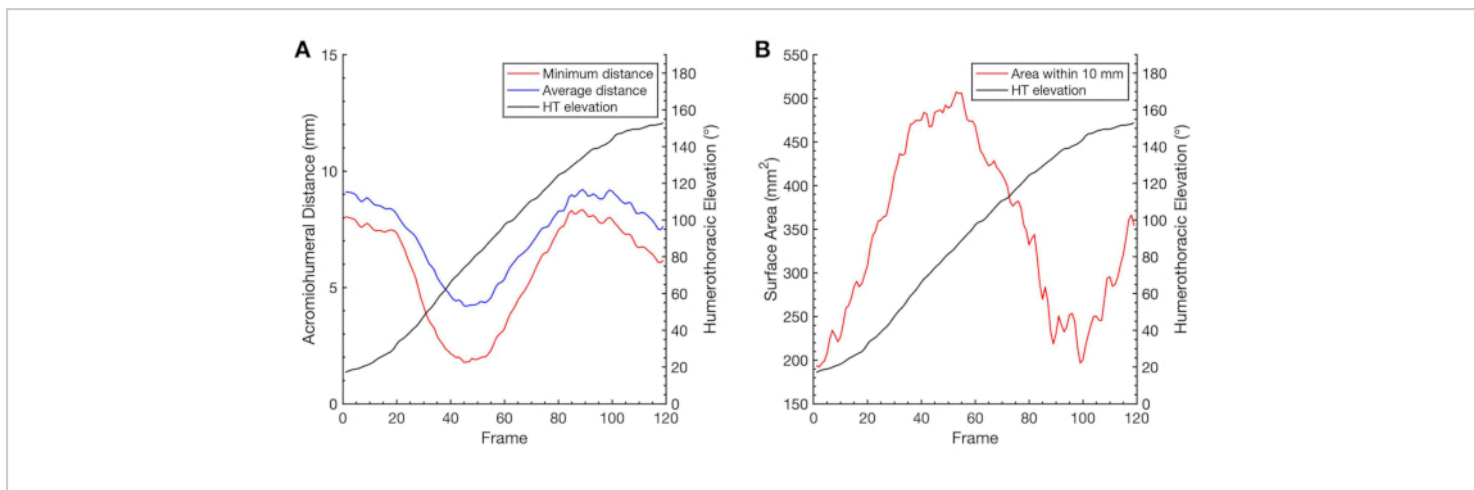


Figure 10: Assessment of the subacromial space during a trial of coronal plane abduction in a representative subject. (A) Measures of acromiohumeral distance are displayed across frames along with the corresponding humerothoracic elevation angles. The minimum distance is calculated as the smallest distance between the centroids of the nearest-neighbor triangle between the humeral head and acromial ROIs. The average distance represents the area-weighted mean of the minimum distance, calculated over the triangles in the humeral head ROI that have the smallest gap to their nearest neighbor on the acromial ROI. (B) The surface area of the humeral head ROI that is within 10 mm of the acromial ROI is displayed across frames along with the corresponding humerothoracic elevation angles. Abbreviation: HT = humerothoracic. [Please click here to view a larger version of this figure.](#)

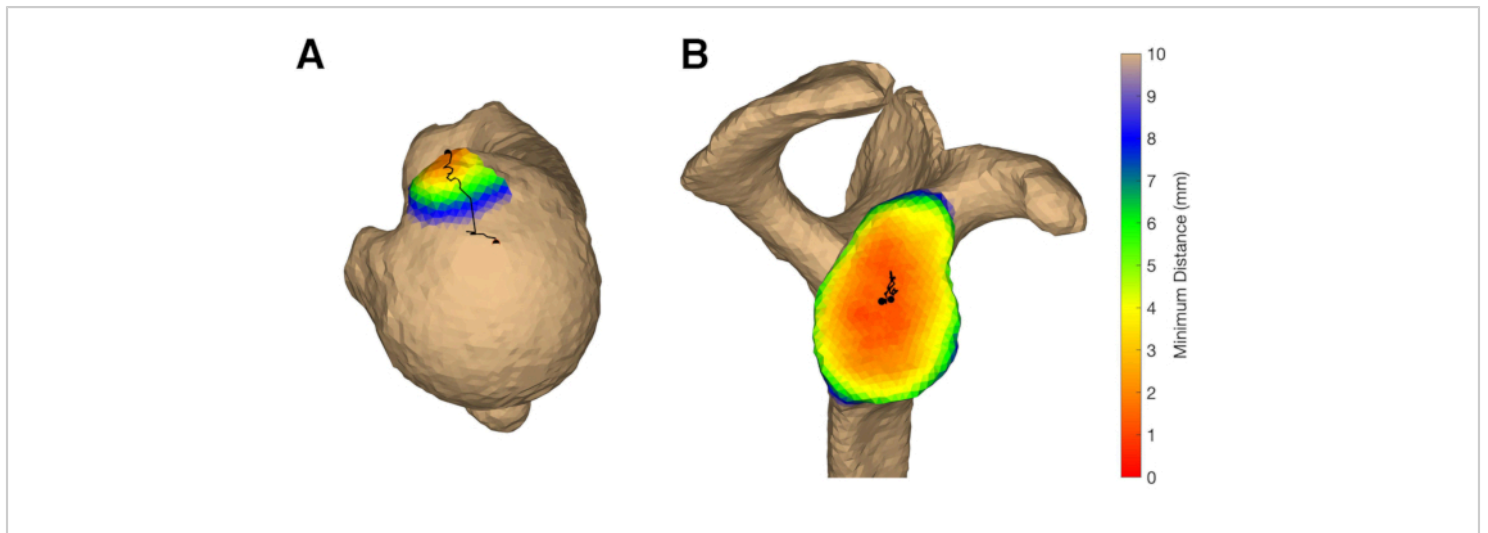


Figure 11: Proximity mapping. (A) subacromial space, (B) glenohumeral joint space. The subacromial proximity is mapped on the humeral head ROI using the minimum distance metric for the frame of data in which the minimum distance was smallest (i.e., frame #45). The contact path (black) represents the minimum distance trajectory between frames #1-45. The glenohumeral joint proximity is mapped using the weighted-average contact center for the frame of data in which the joint space was smallest (i.e., frame #92). The contact path (black) represents the centroid trajectory between frames #1-92.

[Please click here to view a larger version of this figure.](#)

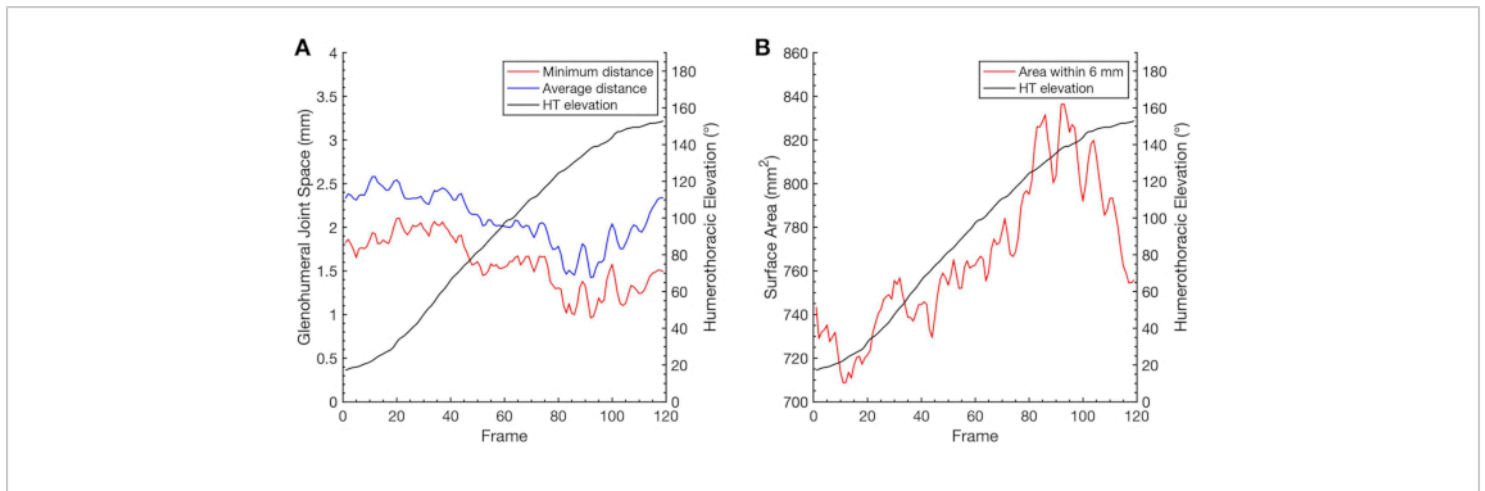


Figure 12: Assessment of the glenohumeral joint space during a trial of coronal plane abduction in a representative subject. (A) Measures of glenohumeral joint space are displayed across frames along with the corresponding humerothoracic elevation angles. The minimum distance is calculated as the smallest distance between the centroids of the nearest-neighbor triangle between the glenoid and humeral head ROIs. The average distance represents the area-weighted mean of the minimum distance, calculated over the triangles in the glenoid ROI that have the smallest gap to their nearest neighbor on the humeral head ROI. (B) The surface area of the glenoid ROI that is within 10 mm of the humeral head ROI is displayed across frames along with the corresponding humerothoracic elevation angles. Abbreviation: HT = humerothoracic. [Please click here to view a larger version of this figure.](#)

Discussion

The technique described here overcomes several disadvantages associated with conventional techniques for assessing shoulder motion (i.e., cadaveric simulations, 2D imaging, static 3D imaging, video-based motion capture systems, wearable sensors, etc.) by providing accurate measures of 3D joint motion during dynamic activities. The accuracy of the protocol described herein was established for the glenohumeral joint against the gold standard of radiostereometric analysis (RSA) to be $\pm 0.5^\circ$ and ± 0.4 mm^{67,68}. Similar protocols have been developed for other joints such as the knee⁶⁹, spine⁷⁰, and foot/ankle⁷¹. Importantly, without a system that is sufficiently accurate, the sample size necessary to detect statistically significant

and clinically potential meaningful differences in joint motion could be prohibitive. Furthermore, this level of accuracy affords the ability to describe potentially important outcome measures such as joint positions and/or translations^{62,72}, arthrokinematics^{72,73,74,75}, subacromial distances^{61,72,75}, and instantaneous axes of motion⁷⁶. Ultimately, accurately measuring in-vivo joint motion is essential for providing a mechanistic understanding of shoulder function under normal and pathologic conditions, and for assessing the effects of non-surgical and surgical clinical interventions.

The accuracy afforded by quantifying shoulder kinematics using biplane videoradiography comes with many challenges and limitations. The primary limitation associated with this technique is the radiation exposure to the participant

as a result of the CT scan and biplane x-ray imaging. Consequently, the number of motion trials that can be acquired or follow-up sessions over time is limited. The effective dose corresponding with the protocol described here is approximately 10.5 mSv, with the majority (approximately 10 mSv) coming from the CT scan, which includes imaging of the distal humerus so that the epicondyles can be used to construct the humeral anatomical coordinate system⁶⁴. For context, this dose corresponds to approximately 3 years of exposure to natural background sources of radiation. Recent recommendations of the National Council on Radiation Protection and Measurements suggest this dose can be classified as "minor" assuming a moderate expected benefit to the individual or society⁷⁷. Consequently, it is imperative that motion analysis using biplane videoradiography be used in a well-designed study based on a solid scientific premise that has the potential to have a significant impact on public health.

Reducing the dose associated with biplane videoradiography is crucial to facilitate the broader use of this technology in research and clinical settings. Fortunately, recent advances in CT and MR imaging may substantially reduce the dose to the participant. For example, humeral and scapular bone models derived using MRI^{78,79} or lower dose CT⁸⁰ have been shown to have acceptable accuracy for many research applications. Furthermore, redefining the humeral coordinate system in a manner that does not require the humeral epicondyles⁸¹ will decrease the dose by reducing the CT imaging volume. Careful practice of motion trials before acquiring any images is also crucial to ensure that each collected trial has value and does not unnecessarily add to the participant's total dose. Ultimately, carefully considering these factors, and many others, is critical when responsibly

using biplane videoradiography to quantify 3D kinematics in human research participants.

The participant's body habitus and differences in tissue density (and therefore image brightness) between the central torso and the lateral aspect of the shoulder presents additional challenges when quantifying shoulder motion using biplane videoradiography. In particular, clear visualization of the scapula and ribs is often challenging using the radiographic technique described in this protocol (i.e., ~70 kVp, 320 mA, 2 ms pulsed exposure) in individuals with high BMI (>30 kg/m²) and women with large or dense breast tissue. Kinematic tracking accuracy likely deteriorates without clear visualization of bone edges. Consequently, careful selection of participants by restricting BMI can ameliorate many of these challenging imaging considerations. However, "washout" of the lateral acromion at lower angles of humeral elevation is common even in participants of healthy body habitus (**Figure 2A**, green system at Frame 1). This is because there is little tissue (and thus density) around the acromion when the humerus is at lower angles of elevation, and visibility of this region is conceded in order to visualize the scapula and ribs. However, once the humerus elevates and the bulk of the shoulder is projected onto itself (thus increasing radiographic density), the acromion becomes well-visualized. Therefore, the optimal radiographic technique for a motion trial does not necessarily guarantee visualization of all bones at all times, but allows for the clear visualization of enough bony anatomy to conduct markerless tracking.

Another challenge when using biplane videoradiography is the relatively small 3D imaging volume, which is predominantly defined by the image receptor size, the orientation of the two imaging systems, and the SID. Although limiting the 3D imaging volume helps control the radiation

dose (i.e., through collimation), a small imaging volume may restrict the range over which joint motion can be acquired and/or the types of tasks being assessed. For example, tasks that require trunk motion (e.g., throwing) may be incompatible with biplane videoradiography motion analysis because the participant will likely move outside of the 3D imaging volume while performing the task. Patient movement outside the imaging volume is common even in simpler tasks such as raising the arm, especially in individuals whose humeral elevation range of motion is significantly impaired (e.g., due to massive rotator cuff tears, adhesive capsulitis, OA), because these individuals often compensate by leaning to the contralateral side. Consequently, careful positioning of the participant within the imaging volume and verbal cues to avoid leaning are crucial steps in the data collection process (section 2.4).

The small 3D imaging volume also limits the visualization of other segments that may be of interest. For example, tracking the torso is necessary to quantify scapulothoracic and humerothoracic kinematics. The protocol described in this article addresses this challenge by tracking the third and fourth ribs. However, other investigators have tracked the torso using an external surface-based tracking system synced with the radiographic system^{49,50,62}. Each of these approaches has unique limitations. For example, tracking the ribs requires good visualization of the central torso, which is challenging in individuals with larger body habitus without washing out the lateral shoulder, as previously described. Furthermore, tracking the ribs may be challenging with a smaller image intensifier (i.e., less than 40 cm). In contrast, tracking torso motion using surface sensors introduces skin motion artifact. Regardless of the approach used, the limited

3D imaging volume remains a challenge when quantifying shoulder kinematics using biplane videoradiography.

In summary, biplane videoradiography allows for highly accurate quantification of shoulder kinematics. Variations in the protocol described herein has been used for numerous studies within the lab^{58,59,72,73,82}, with each protocol variation carefully constructed based on the specific research aims in order to minimize dose, maximize image quality, and maximize segment visibility. Ultimately, accurately measuring in-vivo joint motion is important for providing a mechanistic understanding of shoulder function under normal and pathologic conditions, and for assessing the effects of non-surgical and surgical clinical interventions.

Disclosures

The authors have no conflicts of interest.

Acknowledgments

Research reported in this publication was supported by the National Institute of Arthritis and Musculoskeletal and Skin Diseases under award number R01AR051912. The content is solely the responsibility of the authors and does not necessarily represent the official views of the National Institutes of Health (NIH).

References

1. Milgrom, C., Schaffler, M., Gilbert, S. van Holsbeeck, M. Rotator-cuff changes in asymptomatic adults. The effect of age, hand dominance and gender. *Journal of Bone and Joint Surgery (British Volume)*. **77** (2), 296-298 (1995).
2. Kim, H. M. et al. Location and initiation of degenerative rotator cuff tears: an analysis of three hundred and sixty

- shoulders. *Journal of Bone and Joint Surgery (American Volume)*. **92** (5), 1088-1096 (2010).
3. Yamamoto, A. et al. Prevalence and risk factors of a rotator cuff tear in the general population. *Journal of Shoulder and Elbow Surgery*. **19** (1), 116-120 (2010).
 4. Colvin, A. C., Egorova, N., Harrison, A. K., Moskowitz, A., Flatow, E. L. National trends in rotator cuff repair. *Journal of Bone and Joint Surgery (American Volume)*. **94** (3), 227-233 (2012).
 5. Vitale, M. A. et al. Rotator cuff repair: an analysis of utility scores and cost-effectiveness. *Journal of Shoulder and Elbow Surgery*. **16** (2), 181-187 (2007).
 6. Zacchilli, M. A., Owens, B. D. Epidemiology of shoulder dislocations presenting to emergency departments in the United States. *Journal of Bone and Joint Surgery (American Volume)*. **92** (3), 542-549 (2010).
 7. Oh, J. H. et al. The prevalence of shoulder osteoarthritis in the elderly Korean population: association with risk factors and function. *Journal of Shoulder and Elbow Surgery*. **20** (5), 756-763 (2011).
 8. Kobayashi, T. et al. Prevalence of and risk factors for shoulder osteoarthritis in Japanese middle-aged and elderly populations. *Journal of Shoulder and Elbow Surgery*. **23** (5), 613-619 (2014).
 9. Ludewig, P.M., Reynolds, J. F. The association of scapular kinematics and glenohumeral joint pathologies. *Journal of Orthopaedic and Sports Physical Therapy*. **39** (2), 90-104 (2009).
 10. Michener, L. A., McClure, P. W., Karduna, A. R. Anatomical and biomechanical mechanisms of subacromial impingement syndrome. *Clinical Biomechanics (Bristol, Avon)*. **18** (5), 369-379 (2003).
 11. Seitz, A. L., McClure, P. W., Finucane, S., Boardman, N. D., Michener, L. A. Mechanisms of rotator cuff tendinopathy: intrinsic, extrinsic, or both? *Clinical Biomechanics (Bristol, Avon)*. **26** (1), 1-12 (2011).
 12. Lawrence, R. L., Braman, J. P., Ludewig, P. M. Shoulder kinematics impact subacromial proximities: a review of the literature. *Brazilian Journal of Physical Therapy*. **24** (3), 219-230 (2019).
 13. McClure, P. W., Michener, L. A., Karduna, A. R. Shoulder function and 3-dimensional scapular kinematics in people with and without shoulder impingement syndrome. *Physical Therapy*. **86** (8), 1075-1090 (2006).
 14. Rundquist, P. J. Alterations in scapular kinematics in subjects with idiopathic loss of shoulder range of motion. *Journal of Orthopaedic and Sports Physical Therapy*. **37** (1), 19-25 (2007).
 15. Graichen, H. et al. Effect of abducting and adducting muscle activity on glenohumeral translation, scapular kinematics and subacromial space width in vivo. *Journal of Biomechanics*. **38** (4), 755-760 (2005).
 16. Bey, M. J., Kline, S. K., Zauel, R., Lock, T. R., Kolowich, P. A. Measuring dynamic in-vivo glenohumeral joint kinematics: technique and preliminary results. *Journal of Biomechanics*. **41** (3), 711-714 (2008).
 17. Poppen, N. K., Walker, P. S. Normal and abnormal motion of the shoulder. *Journal of Bone and Joint Surgery (American Volume)*. **58** (2), 195-201 (1976).
 18. Graichen, H. et al. Magnetic resonance-based motion analysis of the shoulder during elevation. *Clinical Orthopaedics and Related Research*. (370), 154-163 (2000).

19. Howell, S. M., Galinat, B. J., Renzi, A. J., Marone, P. J. Normal and abnormal mechanics of the glenohumeral joint in the horizontal plane. *Journal of Bone and Joint Surgery (American Volume)*. **70** (2), 227-232 (1988).
20. Bergmann, G. et al. In vivo glenohumeral contact forces--measurements in the first patient 7 months postoperatively. *Journal of Biomechanics*. **40** (10), 2139-2149 (2007).
21. Westerhoff, P. et al. In vivo measurement of shoulder joint loads during activities of daily living. *Journal of Biomechanics*. **42** (12), 1840-1849 (2009).
22. Bergmann, G. et al. In vivo gleno-humeral joint loads during forward flexion and abduction. *Journal of Biomechanics*. **44** (8), 1543-1552 (2011).
23. Halder, A. M., Zhao, K. D., Odriscoll, S. W., Morrey, B. F., An, K. N. Dynamic contributions to superior shoulder stability. *Journal of Orthopaedic Research*. **19** (2), 206-212 (2001).
24. Debski, R. E. et al. A new dynamic testing apparatus to study glenohumeral joint motion. *Journal of Biomechanics*. **28** (7), 869-874 (1995).
25. Malicky, D. M., Soslowky, L. J., Blasler, R. B., Shyr, Y. Anterior glenohumeral stabilization factors: progressive effects in a biomechanical model. *Journal of Orthopaedic Research*. **14** (2), 282-288 (1996).
26. Payne, L. Z., Deng, X. H., Craig, E. V., Torzilli, P. A., Warren, R. F. The combined dynamic and static contributions to subacromial impingement. A biomechanical analysis. *American Journal of Sports Medicine*. **25** (6), 801-808 (1997).
27. Wuelker, N., Wirth, C. J., Plitz, W., Roetman, B. A dynamic shoulder model: reliability testing and muscle force study. *Journal of Biomechanics*. **28** (5), 489-499 (1995).
28. Dillman, C. J., Fleisig, G. S., Andrews, J. R. Biomechanics of pitching with emphasis upon shoulder kinematics. *Journal of Orthopaedic and Sports Physical Therapy*. **18** (2), 402-408 (1993).
29. Fleisig, G. S., Andrews, J. R., Dillman, C. J., Escamilla, R. F. Kinetics of baseball pitching with implications about injury mechanisms. *American Journal of Sports Medicine*. **23** (2), 233-239 (1995).
30. Fleisig, G. S., Barrentine, S. W., Zheng, N., Escamilla, R. F., Andrews, J. R. Kinematic and kinetic comparison of baseball pitching among various levels of development. *Journal of Biomechanics*. **32** (12), 1371-1375 (1999).
31. Werner, S. L., Gill, T. J., Murray, T. A., Cook, T. D., Hawkins, R. J. Relationships between throwing mechanics and shoulder distraction in professional baseball pitchers. *American Journal of Sports Medicine*. **29** (3), 354-358 (2001).
32. An, K. N., Browne, A. O., Korinek, S., Tanaka, S., Morrey, B. F. Three-dimensional kinematics of glenohumeral elevation. *Journal of Orthopaedic Research*. **9** (1), 143-149 (1991).
33. Johnson, M. P., McClure, P. W., Karduna, A. R. New method to assess scapular upward rotation in subjects with shoulder pathology. *Journal of Orthopaedic and Sports Physical Therapy*. **31** (2), 81-89 (2001).
34. Borstad, J. D., Ludewig, P. M. Comparison of scapular kinematics between elevation and lowering of the arm in the scapular plane. *Clinical Biomechanics (Bristol, Avon)*. **17** (9-10), 650-659 (2002).

35. Meskers, C. G., van der Helm, F. C., Rozendaal, L. A., Rozing, P. M. In vivo estimation of the glenohumeral joint rotation center from scapular bony landmarks by linear regression. *Journal of Biomechanics*. **31** (1), 93-96 (1998).
36. McClure, P. W., Michener, L. A., Sennett, B. J., Karduna, A. R. Direct 3-dimensional measurement of scapular kinematics during dynamic movements in vivo. *Journal of Shoulder and Elbow Surgery*. **10** (3), 269-277 (2001).
37. Lawrence, R. L., Braman, J. P., LaPrade, R. F., Ludewig, P.M. Comparison of 3-dimensional shoulder complex kinematics in individuals with and without shoulder pain, part 1: sternoclavicular, acromioclavicular, and scapulothoracic joints. *Journal of Orthopaedic and Sports Physical Therapy*. **44** (9), 636-645, A631-638 (2014).
38. Lawrence, R. L., Braman, J. P., Staker, J. L., LaPrade, R. F., Ludewig, P. M. Comparison of 3-dimensional shoulder complex kinematics in individuals with and without shoulder pain, part 2: glenohumeral joint. *Journal of Orthopaedic and Sports Physical Therapy*. **44** (9), 646-655, B641-643 (2014).
39. Burkhart, S. S. Fluoroscopic comparison of kinematic patterns in massive rotator cuff tears. A suspension bridge model. *Clinical Orthopaedics and Related Research*. **284**, 144-152 (1992).
40. Mandalidis, D. G., Mc Glone, B. S., Quigley, R. F., McInerney, D., O'Brien, M. Digital fluoroscopic assessment of the scapulohumeral rhythm. *Surgical and Radiologic Anatomy*. **21** (4), 241-246 (1999).
41. Pfirrmann, C. W., Huser, M., Szekely, G., Hodler, J., Gerber, C. Evaluation of complex joint motion with computer-based analysis of fluoroscopic sequences. *Investigative Radiology*. **37** (2), 73-76 (2002).
42. Deutsch, A., Altchek, D. W., Schwartz, E., Otis, J. C., Warren, R. F. Radiologic measurement of superior displacement of the humeral head in the impingement syndrome. *Journal of Shoulder and Elbow Surgery*. **5** (3), 186-193 (1996).
43. Hawkins, R. J., Schutte, J. P., Janda, D. H., Huckell, G. H. Translation of the glenohumeral joint with the patient under anesthesia. *Journal of Shoulder and Elbow Surgery*. **5** (4), 286-292 (1996).
44. Yamaguchi, K. et al. Glenohumeral motion in patients with rotator cuff tears: a comparison of asymptomatic and symptomatic shoulders. *Journal of Shoulder and Elbow Surgery*. **9** (1), 6-11 (2000).
45. Paletta, G. A. Jr., Warner, J. J., Warren, R. F., Deutsch, A., Altchek, D. W. Shoulder kinematics with two-plane x-ray evaluation in patients with anterior instability or rotator cuff tearing. *Journal of Shoulder and Elbow Surgery*. **6** (6), 516-527 (1997).
46. Graichen, H. et al. Three-dimensional analysis of the width of the subacromial space in healthy subjects and patients with impingement syndrome. *AJR: American Journal of Roentgenology*. **172** (4), 1081-1086 (1999).
47. Rhoad, R. C. et al. A new in vivo technique for three-dimensional shoulder kinematics analysis. *Skeletal Radiology*. **27** (2), 92-97 (1998).
48. Baeyens, J. P., Van Roy, P., De Schepper, A., Declercq, G., Clarijs, J. P. Glenohumeral joint kinematics related to minor anterior instability of the shoulder at the end of the late preparatory phase of throwing. *Clinical Biomechanics (Bristol, Avon)*. **16** (9), 752-757 (2001).

49. Lawrence, R. L., Braman, J. P., Keefe, D. F., Ludewig, P. M. The Coupled Kinematics of Scapulothoracic Upward Rotation. *Physical Therapy*. **100** (2), 283-294 (2020).
50. Lawrence, R. L., Braman, J. P., Ludewig, P. M. The impact of decreased scapulothoracic upward rotation on subacromial proximities. *Journal of Orthopaedic and Sports Physical Therapy*. **49** (3), 180-191 (2019).
51. Matsuki, K. et al. Dynamic in vivo glenohumeral kinematics during scapular plane abduction in healthy shoulders. *Journal of Orthopaedic and Sports Physical Therapy*. **42** (2), 96-104 (2012).
52. Chapman, R. M., Torchia, M. T., Bell, J. E., Van Citters, D. W. Assessing shoulder biomechanics of healthy elderly individuals during activities of daily living using inertial measurement units: High maximum elevation is achievable but rarely used. *Journal of Biomechanical Engineering*. **141** (4) (2019).
53. De Baets, L., van der Straaten, R., Matheve, T., Timmermans, A. Shoulder assessment according to the international classification of functioning by means of inertial sensor technologies: A systematic review. *Gait and Posture*. **57**, 278-294 (2017).
54. Dowling, B., McNally, M. P., Laughlin, W. A., Onate, J. A. Changes in throwing arm mechanics at increased throwing distances during structured long-toss. *American Journal of Sports Medicine*. **46** (12), 3002-3006 (2018).
55. Kirking, B., El-Gohary, M., Kwon, Y. The feasibility of shoulder motion tracking during activities of daily living using inertial measurement units. *Gait and Posture*. **49**, 47-53 (2016).
56. Morrow, M. M. B., Lowndes, B., Fortune, E., Kaufman, K. R., Hallbeck, M. S. Validation of inertial measurement units for upper body kinematics. *Journal of Applied Biomechanics*. **33** (3), 227-232 (2017).
57. Rawashdeh, S. A., Rafeldt, D. A., Uhl, T. L. Wearable IMU for shoulder injury prevention in overhead sports. *Sensors (Basel)*. **16** (11) (2016).
58. Baumer, T. G. et al. Effects of asymptomatic rotator cuff pathology on in vivo shoulder motion and clinical outcomes. *Journal of Shoulder and Elbow Surgery*. **26** (6), 1064-1072 (2017).
59. Bey, M. J. et al. In vivo measurement of subacromial space width during shoulder elevation: technique and preliminary results in patients following unilateral rotator cuff repair. *Clinical Biomechanics (Bristol, Avon)*. **22** (7), 767-773 (2007).
60. Peltz, C. D. et al. Differences in glenohumeral joint morphology between patients with anterior shoulder instability and healthy, uninjured volunteers. *Journal of Shoulder and Elbow Surgery*. **24** (7), 1014-1020 (2015).
61. Coats-Thomas, M. S., Massimini, D. F., Warner, J. J. P., Seitz, A. L. In vivo evaluation of subacromial and internal impingement risk in asymptomatic individuals. *American Journal of Physical Medicine and Rehabilitation*. **97** (9), 659-665 (2018).
62. Millett, P. J., Giphart, J. E., Wilson, K. J., Kagnes, K., Greenspoon, J. A. Alterations in glenohumeral kinematics in patients with rotator cuff tears measured with biplane fluoroscopy. *Arthroscopy*. **32** (3), 446-451 (2016).
63. Li, W., Hou, Q. Analysis and correction of the nonuniformity of light field in the high resolution X-ray digital radiography. *Sixth International Conference on Natural Computation*. **7**, 3803-3807 (2010).

64. Wu, G. et al. ISB recommendation on definitions of joint coordinate systems of various joints for the reporting of human joint motion--Part II: shoulder, elbow, wrist and hand. *Journal of Biomechanics*. **38** (5), 981-992 (2005).
65. Baumer, T. G. et al. Effects of rotator cuff pathology and physical therapy on in vivo shoulder motion and clinical outcomes in patients with a symptomatic full-thickness rotator cuff tear. *Orthopaedic Journal of Sports Medicine*. **4** (9), 2325967116666506 (2016).
66. Ludewig, P. M. et al. Motion of the shoulder complex during multiplanar humeral elevation. *Journal of Bone and Joint Surgery (American Volume)*. **91** (2), 378-389 (2009).
67. Bey, M. J., Zael, R., Brock, S. K., Tashman, S. Validation of a new model-based tracking technique for measuring three-dimensional, in vivo glenohumeral joint kinematics. *Journal of Biomechanical Engineering*. **128** (4), 604-609 (2006).
68. Tashman, S., Anderst, W. In-vivo measurement of dynamic joint motion using high speed biplane radiography and CT: application to canine ACL deficiency. *Journal of Biomechanical Engineering*. **125** (2), 238-245 (2003).
69. Anderst, W., Zael, R., Bishop, J., Demps, E., Tashman, S. Validation of three-dimensional model-based tibio-femoral tracking during running. *Medical Engineering and Physics*. **31** (1), 10-16 (2009).
70. Kage, C. C. et al. Validation of an automated shape-matching algorithm for biplane radiographic spine osteokinematics and radiostereometric analysis error quantification. *PloS One*. **15** (2), e0228594 (2020).
71. Pitcairn, S., Kromka, J., Hogan, M., Anderst, W. Validation and application of dynamic biplane radiography to study in vivo ankle joint kinematics during high-demand activities. *Journal of Biomechanics*. **103**, 109696 (2020).
72. Bey, M. J. et al. In vivo shoulder function after surgical repair of a torn rotator cuff: glenohumeral joint mechanics, shoulder strength, clinical outcomes, and their interaction. *American Journal of Sports Medicine*. **39** (10), 2117-2129 (2011).
73. Peltz, C. D. et al. Associations between in-vivo glenohumeral joint motion and morphology. *Journal of Biomechanics*. **48** (12), 3252-3257 (2015).
74. Massimini, D. F., Warner, J. J., Li, G. Glenohumeral joint cartilage contact in the healthy adult during scapular plane elevation depression with external humeral rotation. *Journal of Biomechanics*. **47** (12), 3100-3106 (2014).
75. Miller, R. M. et al. Effects of exercise therapy for the treatment of symptomatic full-thickness supraspinatus tears on in vivo glenohumeral kinematics. *Journal of Shoulder and Elbow Surgery*. **25** (4), 641-649 (2016).
76. Lawrence, R. L., Ruder, M. C., Zael, R., Bey, M. J. Instantaneous helical axis estimation of glenohumeral kinematics: The impact of rotator cuff pathology. *Journal of Biomechanics*. **109** 109924 (2020).
77. National Council on Radiation Protection and Measurements. *Evaluating and communicating radiation risks for studies involving human subjects: guidance for researchers and institutional review boards: recommendations of the National Council on Radiation Protection and Measurements*. National Council on Radiation Protection and Measurements (2020).

78. Akbari-Shandiz, M. et al. MRI vs CT-based 2D-3D auto-registration accuracy for quantifying shoulder motion using biplane video-radiography. *Journal of Biomechanics*. **82** 30385001 (2019).
79. Breighner, R. E. et al. Technical developments: Zero echo time imaging of the shoulder: enhanced osseous detail by using MR imaging. *Radiology*. **286** (3), 960-966 (2018).
80. Fox, A. M. et al. The effect of decreasing computed tomography dosage on radiostereometric analysis (RSA) accuracy at the glenohumeral joint. *Journal of Biomechanics*. **44** (16), 2847-2850 (2011).
81. Lawrence, R. L. et al. Effect of glenohumeral elevation on subacromial supraspinatus compression risk during simulated reaching. *Journal of Orthopaedic Research*. **35** (10), 2329-2337 (2017).
82. Peltz, C. D. et al. Associations among shoulder strength, glenohumeral joint motion, and clinical outcome after rotator cuff repair. *American Journal of Orthopedics (Belle Mead, N.J.)*. **43** (5), 220-226 (2014).